PHILOSOPHICAL TRANSACTIONS OF THE ROYAL SOCIETY A MATHEMATICAL, PHYSICAL & ENGINEERING SCIENCES

OPAL Detector Performance

A. Michelini

Phil. Trans. R. Soc. Lond. A 1991 **336**, 237-246
doi: 10.1098/rsta.1991.0076

OPAL detector performance

By A. Michelini
CERN EP, Geneva 23, Switzerland

This paper describes some of the present results on detector performances obtained from the analysis of the data collected by the OPAL experiment during the year 1990 at the CERN e^+e^- LEP accelerator.

1. Introduction

This paper describes some of the OPAL detector performances as they currently emerge from the current data analysis. OPAL (see figure 1) is one of the four experiments installed at the LEP e^+e^- accelerator of CERN. Both the LEP accelerator and the OPAL experiments have been described in LEP (1984) and OPAL (1991).

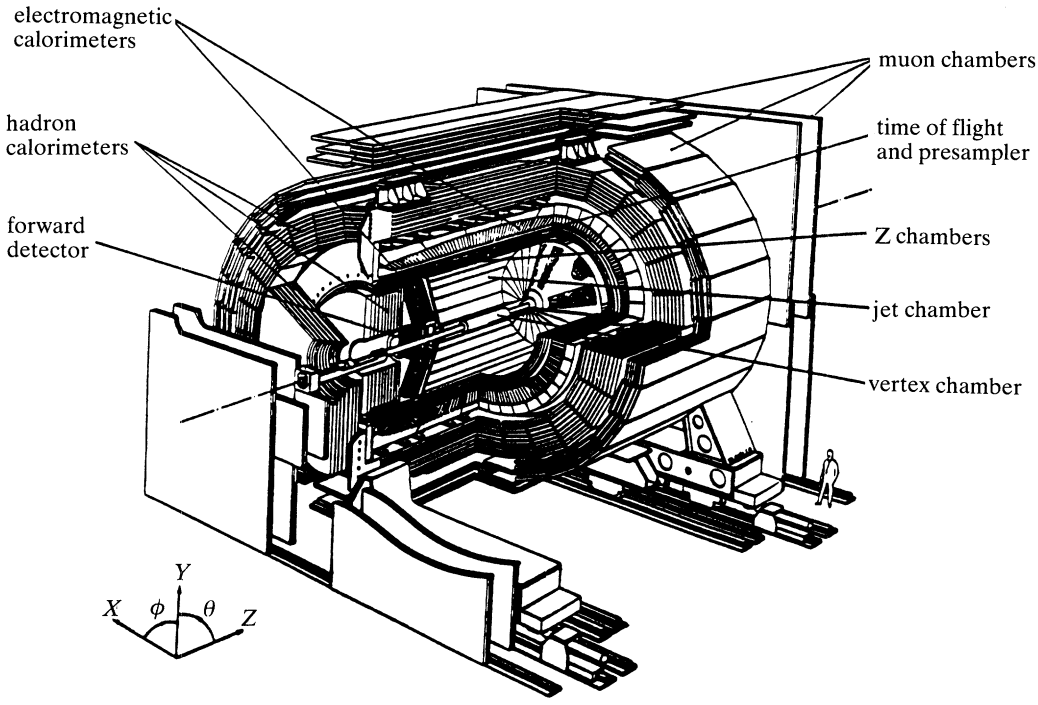

Figure 1. Isometric view of the OPAL experiment.

Section 2 deals with the performance of the central tracking detector. The corresponding resolutions refer to measurements of spatial coordinates, fractional energy dE/dx deposited in the detector gas by charged particles, the track impact parameter and the multiparticle effective mass. In §3 some aspects of the

Phil. Trans. R. Soc. Lond. A (1991) **336**, 237–246
Printed in Great Britain

measurement of the radiative decay of Z^0s into neutrino–antineutrino pairs (CERN 1991) are shown to illustrate some characteristic features of the electromagnetic calorimeter when involving the detection of low-energy single photons and in the presence of heavy background produced from radiative e^+e^- small-angle scattering. Section 4 deals with the reconstruction of the total visible energy for events with Z^0s decaying into hadronic jets. In §5 the identification of single electrons produced inside jets is illustrated as an example of optimization of the electron signal with respect to background, requiring the combination of information from various detectors.

2. The central tracking detector

The central tracking detector consists of three drift chambers mounted as one unit inside a common vessel operated at 4 bar (0.4 MPa) with a gas mixture of Ar, 9.8% methane, 2% isobutane. Two cylindrical coaxial chambers (vertex CV, jet CJ) have the electrical drift field oriented perpendicular to the electron beam axis to provide best space point measurements in the $R\phi$ plane, perpendicular to the beam axis.

The third drift chamber (CZ) is a multicell time projection chamber, mounted all around the CJ chamber at its outer radius. CZ is meant to provide accurate measurements of the axial coordinate. A solenoidal coil generates a uniform axial field of 0.43 T inside the 75 m^3 volume of the central detector. In table 1 are listed the best values obtained for the space, momentum and dE/dx resolutions.

Table 1. *Central detector best measured resolutions*

(Space resolutions are in the $R\phi$ plane for CV and CJ and in the RZ plane for CZ (Z is parallel to the beam axis direction). The momentum resolution is obtained by combining the measurements from the three detectors: CV, CJ, CZ. The dE/dx resolution refers to tracks which collect in CJ the maximum number (i.e. 159) of wire hits.)

	CV	CJ	CZ
radius/m	0.23	0.23–2.0	~ 2.0
best space resolution/μm	50	120	500
$\sigma p/p^2/(\mathrm{GeV}/c)^{-1}$	—	1.51×10^{-3}	—
$[\sigma(dE/dx)]/[dE/dx]$	—	$3\text{–}4 \times 10^{-2}$	—

The quoted momentum resolution is obtained from residual measurements of the quantity Q/p, $Q = \pm 1$ being the charge sign, and using Z^0 decays in pairs of muons, each with a momentum of 45 GeV/c.

Particle identification by dE/dx can be demonstrated using tracks from Z^0 decays into hadronic jets with the requirement of more than 40 dE/dx samples measured per track. Figure 2 shows the actual particle separation as defined by the difference between two particles dE/dx, in units of dE/dx standard deviations, σ.

As it can be seen, separation in excess of 2σ can be obtained for e/π up to a momentum of 11 GeV/c and for π/K up to 13 GeV/c. Separations in excess of 1.5σ is obtained for K/p between 7 and 13 GeV/c.

Space accuracy in the region close to the detector origin can be estimated by measuring the miss distance between two fitted tracks at the point of closest approach, both in the $R\phi$ and RZ planes. The miss distance distribution is shown in

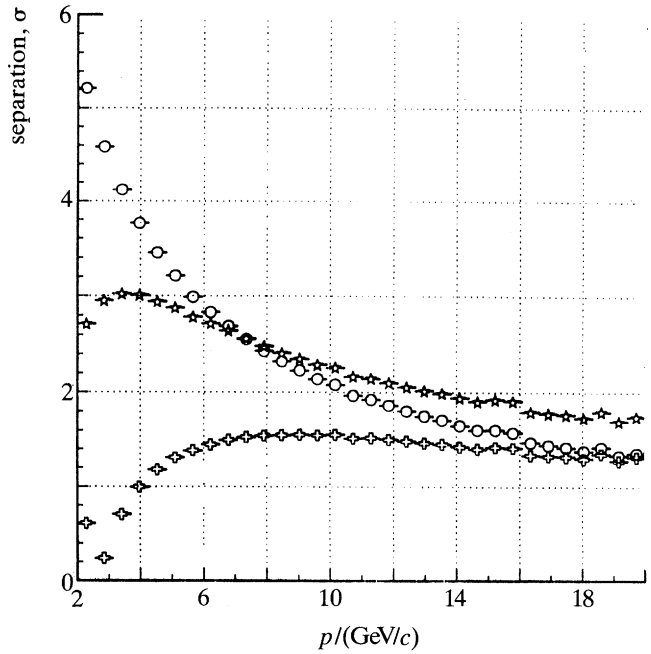

Figure 2. Particle separation power, OPAL. ○, e–π; ☆, π-K; ✧, K–p.

Figure 3

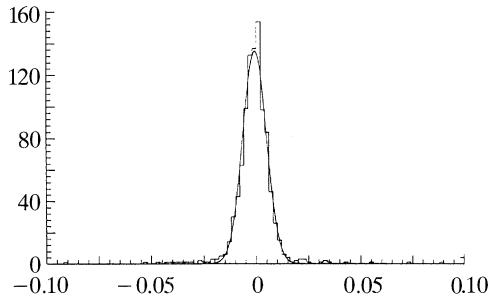

Figure 4

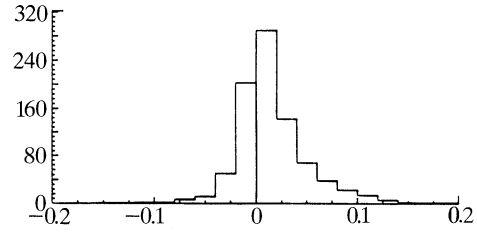

Figure 3. Miss distance (cm) between tracks in $r\phi$ plane. Tracks from $Z^0 \rightarrow$ lepton pairs; $\sigma = 57$ μm.
Figure 4. Electron signed impact parameter (cm).

figure 3 for Z^0 decays into pairs of electrons and muons with a momentum greater than 20 GeV/c. Value of σ of 57 μm is obtained for the plane $R\phi$ using data from CV, CJ and CZ detectors. The corresponding estimate of the impact parameter resolution σ_δ can be derived from the relation: $\sigma_\delta = \sigma/\sqrt{2}$.

Accurate tracking allows measurements of short lifetimes corresponding to decay paths of fractions of a millimetre as in the case of B-mesons. Figure 4 shows results from the measurement of the signed impact parameter δ for electrons of transverse momentum greater than 1 GeV/c contained in jets from Z^0 decays.

A clear asymmetric distribution is visible with excess of positive values of δ originated from B decays.

The feasibility of measuring directly the B-lifetime from the decay length in the

Figure 5

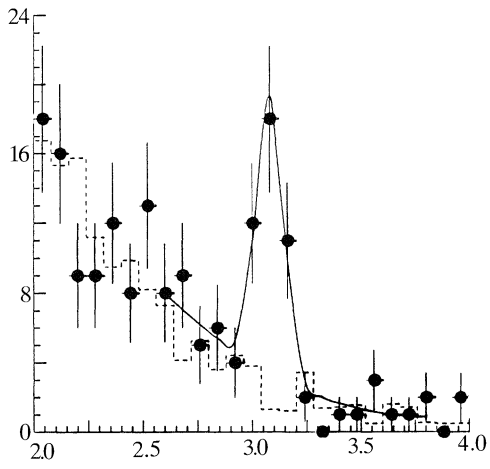

Figure 6

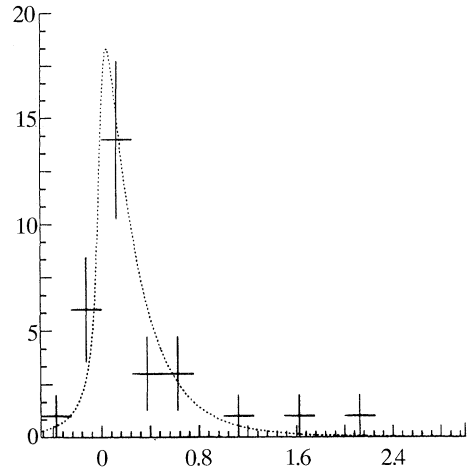

Figure 5. $\mu^+\mu^-$ mass distribution (GeV/c^2).

Figure 6. Decay length (cm).

decay channel $B \rightarrow J/\psi + X$ and subsequent decay of J/ψ into a muon pair is illustrated in figures 5 and 6.

Figure 5 shows the effective mass distribution for a selected sample of unlike sign dimuon events and the presence of a clear J/ψ peak.

The corresponding measured decay length distribution (figure 6) for dimuon selected in the mass interval 2.95 to 3.30 GeV/c^2 and with a total momentum greater than 10 GeV, shows compatibility with Monte Carlo expectation based on an exponential decay distribution (dotted curve) from B decay.

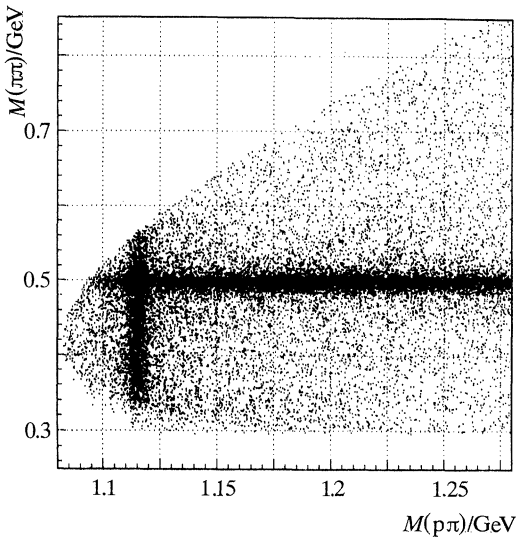

Figure 7. Effective mass Dalitz plot. $M(\pi\pi)$ against $M(p\pi)$, no dE/dx cuts.

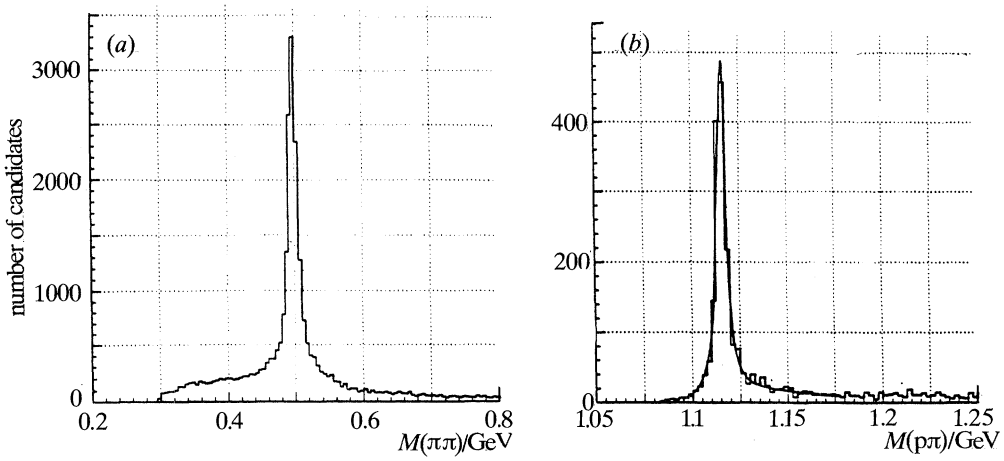

Figure 8. Projection of Dalitz plot (see figure 7): (*a*) on the $\pi^+\pi^-$ axis (no dE/dx cuts); (*b*) on the $p\pi^-$ axis, after applying dE/dx constraints to select positive secondaries as protons.

Further illustration of accurate tracking resolution is provided by identification of K^0, Λ^0, ϕ, D* particles.

Figure 7 shows a Dalitz plot of the $\pi^+\pi^-$ against $p\pi^-$ effective mass measurements. K^0 and Λ^0 bands are clearly visible.

The corresponding projections on $\pi^+\pi^-$ and $p\pi^-$ axis are shown in figure 8*a*, *b*. By applying dE/dx constraints on the selection of $\Lambda^0 \rightarrow p\pi^-$, a Λ^0 signal is obtained (figure 8*b*) with much improved signal/background ratio. The resulting mass resolutions for K^0 and Λ^0 are 6.1 MeV and 2.2 MeV respectively.

Figure 9

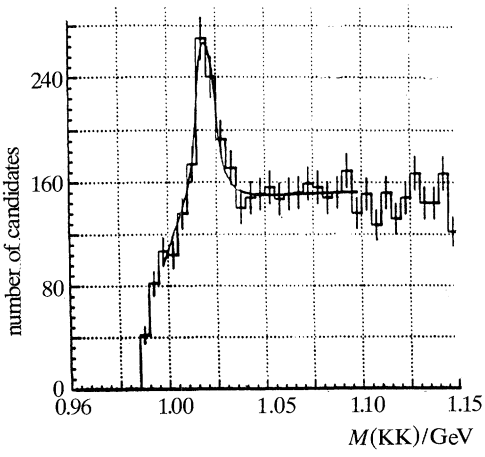

Figure 9. M(KK), with dE/dx cuts. $x^1 = 0.7598$.

Figure 10

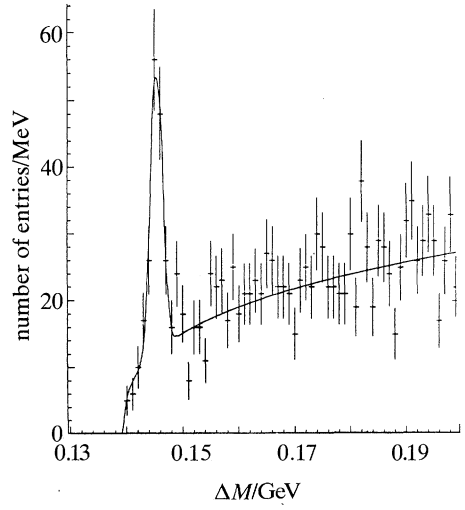

Figure 10. Mass difference $\Delta M = M^*_D - M^0_D$. +, Data for $x_D > 0$. Function: fit to data.

The measurement of dE/dx in identifying $K^{\pm}$ particles allows to isolate a $\phi \to K^+K^-$ signal as shown in figure 9. The obtained ϕ mass resolution is 9.8 MeV.

Finally accurate tracking is required to extract a D* signal. Its presence is revealed by a narrow peak (1 MeV/bin, see figure 10) in the mass difference $\Delta M = M^*_D - M^0_D$.

3. The electromagnetic calorimeter

The OPAL electromagnetic calorimeter consists of an array of approximately 12000 lead glass blocks (LG) (figure 11) mounted in one barrel and two end caps thus covering hermetically the full solid angle around the interaction point (IP).

The central detector pressure vessel and end cones, the coil and the time-of-flight scintillator hodoscope (TOF) mounted around the coil are located in front of the lead glass array, thus representing a non-negligible absorber, whose effective thickness is estimated to be $1.8\times$ radiation length at normal incident angles. Photons and electrons, traversing the absorber have a high probability (*ca.* 80%) of conversion before reaching the lead glass detector.

To control the amount of energy deposited in the absorber a presampler detector (PRES) sensitive to charged particles is mounted between the absorber and the lead glass. The measured particle multiplicity in the presampler shows a clear correlation

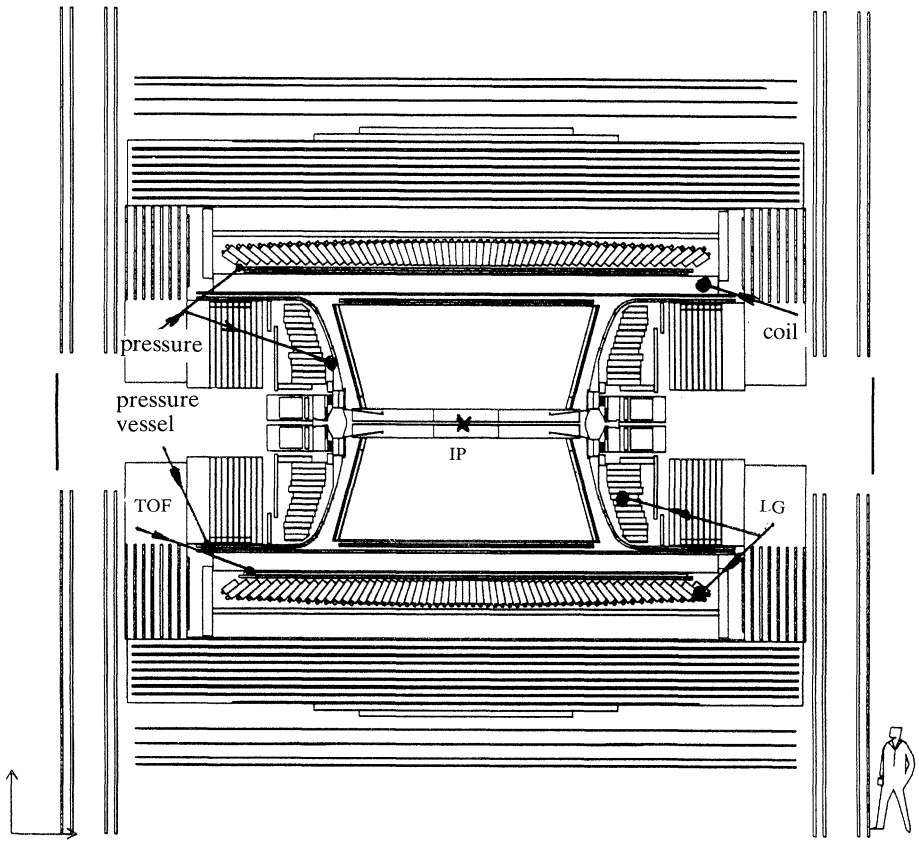

Figure 11. OPAL layout in the XZ plane.

to the energy deposited in the absorber. The total energy measured in the electromagnetic calorimeter for electrons and photons can thus be corrected. The resulting energy resolution obtained for Z^0s into electron pairs is 2.6% at $E = 45$ GeV. Some aspects of the electromagnetic calorimeter performance can be illustrated by a recent OPAL measurement of Z^0 decaying into a neutrino–antineutrino pair associated with a radiative photon (CERN 1991), also called single photon events.

The trigger efficiencies for two types of trigger requirements are shown in figure 12, as determined by using single electron events. Solid triangles refer to lower energy threshold which require a TOF signal coincident to the energy cluster. Full efficiency is reached at 1.4 GeV for the low threshold trigger and correspondingly 3 GeV for the high threshold. Both triggers require conversion in the absorber signalled by a presampler pulse.

The energy spectrum of clusters generated by accidental noise and associated with

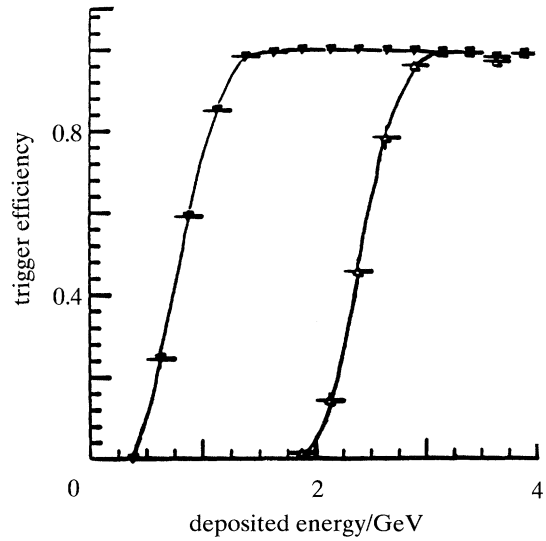

Figure 12. Trigger efficiency against deposited energy in the electromagnetic calorimeter.

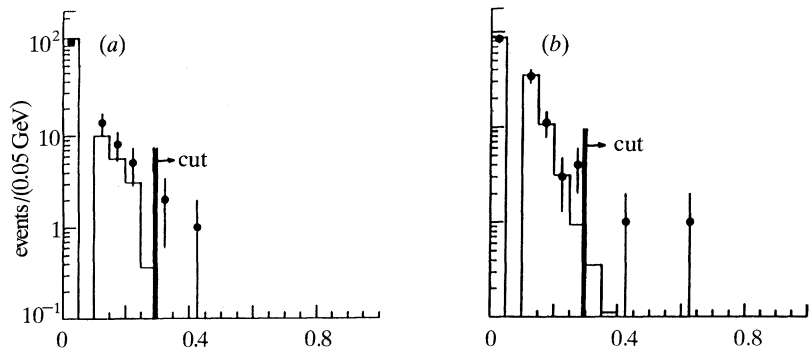

Figure 13. Measured energy spectrum (solid points) of accidental clusters associated to single photon events: (*a*) in the electromagnetic calorimeter barrel; (*b*) in the electromagnetic calorimeter end caps.

single photon events is shown in figure 13. The measured spectrum (solid points) agrees very well with the energy spectrum (solid line) directly measured from random triggers collected at beam crossings.

4. Total visible energy

The measurement of the total visible energy is performed by combining the central detector momentum measurements with the deposited energy both in the electromagnetic and the hadron calorimeter.

The main purpose of the hadron calorimeter is to detect energy clusters deposited by neural hadrons which escape detection in the electromagnetic calorimeter. An example of an event with large portion of neutral hadronic energy is shown in figure 14. The spectrum of total measured visible energy is shown in figure 15. The estimate of the overall resolution is $\sigma_E/E = 12\,\%$.

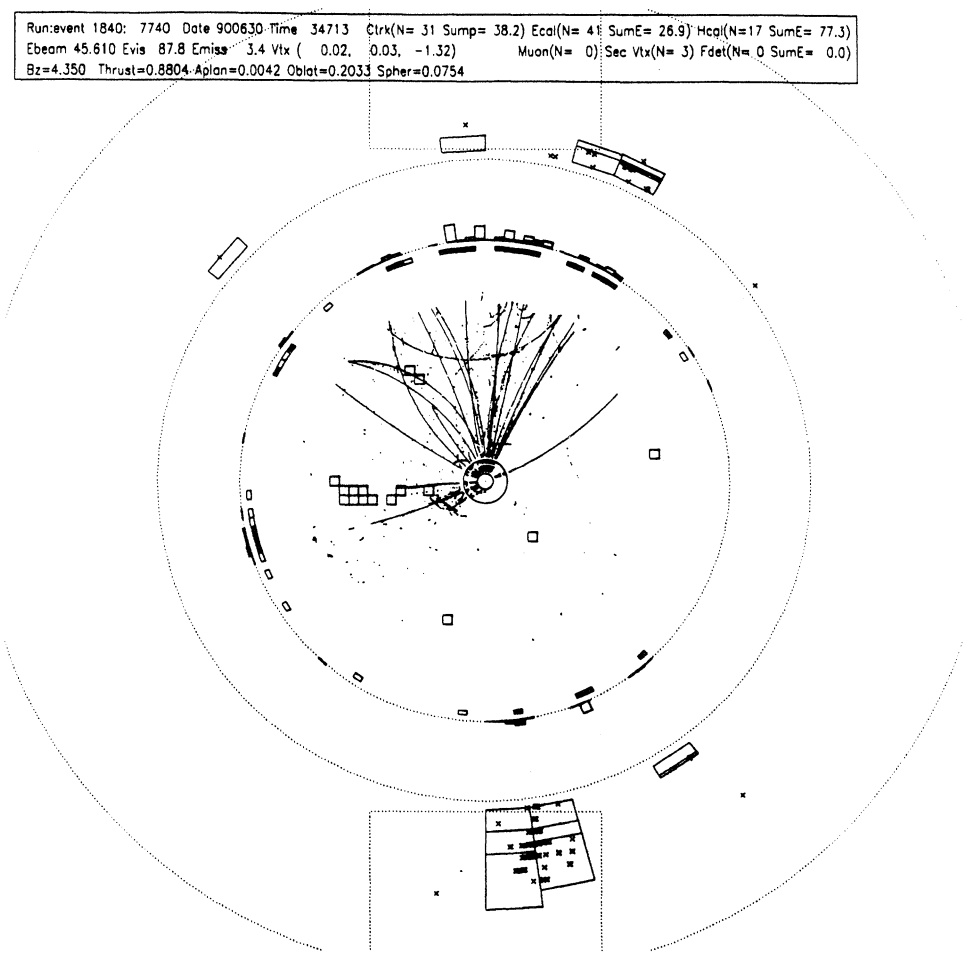

Figure 14. In the shown event the hadronic jet points to the top of the figure and it is balanced at the bottom by a large energy cluster deposited in the hadron calorimeter.

5. Electron identification

An example of electron identification with high purity is shown in figure 16 for momenta between 2 and 4 GeV. An electron peak centred at 10 keV cm^{-1} is clearly separated from an adjacent π peak and a K shoulder. Monte Carlo simulation represented by dotted curves allow to precisely determine the fraction of π contamination of the electron sample.

Figure 15

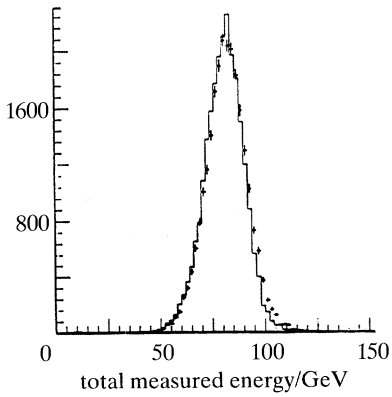

Figure 16

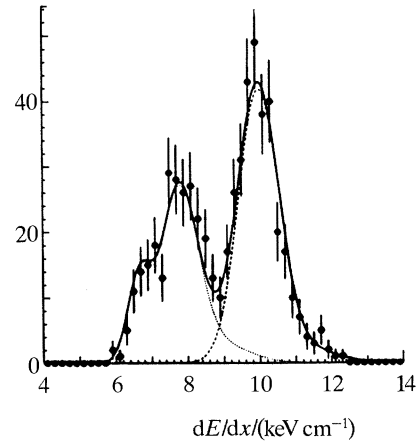

Figure 15. Energy spectrum (solid points) of Z^0 to multihadron events, for well-contained events inside the OPAL detector. The histogram represents the corresponding Monte Carlo simulation.

Figure 16. Electron identification by dE/dx. Electron events are peaked at dE/dx equals 10 keV cm^{-1}. $2 < p < 4$ GeV/c.

Finally electron identification can be obtained by measuring the energy/momentum ratio and applying subsequent selection criteria using different detector information is shown in figure 17*a–d*. Starting with (*a*) simple track resolution requirements, (*b*) the signal purity improves by adding constraints from the presampler detector, (*c*) then from dE/dx, (*d*) and finally requiring a transverse momentum greater than 0.8 GeV/c.

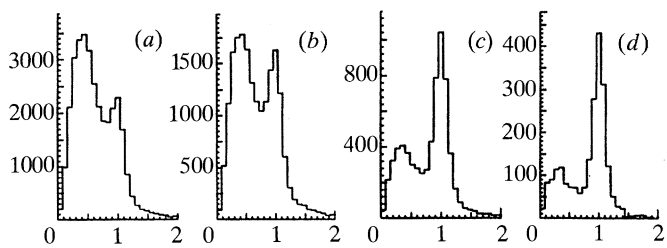

Figure 17. Energy over momentum ratio for jet tracks showing electrons, around one, being discriminated against background. (*a*) E/p–ISOL cuts; (*b*) E/p, add presampler cuts; (*c*) E/p, add 9 dE/dx, 12 keV cm^{-1}; (*d*) E/p, add 0.8 GeV/c.

References

LEP 1984 LEP Design Report. CERN-LEP/84-01, June 1984.

OPAL 1991 The OPAL detector at LEP. CERN PPE/90-114, August 1990. *Nucl. Instrum. Methods.* (Submitted.)

CERN 1991 A direct measurement of the Z^0 invisible width by single photon counting. CERN PPE/90-187, December 1990. *Z. Phys.* C. (Submitted.)

PHILOSOPHICAL TRANSACTIONS OF THE ROYAL SOCIETY A MATHEMATICAL, PHYSICAL & ENGINEERING SCIENCES